International Journal for Housing Science and Its Applications

Publish September 9, 2025. Volume 47, Issue 1 Pages 769-782

https://doi.org/10.70517/ijhsa47167

Enhancing the Control of Tethered Turbofan Rescue Drones Based on Improved Active Disturbance Rejection Control

Jiayi Liu[1,*]

[1] School of Science, Qingdao University of Technology, Qingdao, Shandong, 266520, China

Corresponding authors: (e-mail: liujiayi61777@163.com).

Abstract To address rescue challenges caused by material shortages, traffic disruptions, and complex terrain in disaster zones, this study proposes a tethered turbojet UAV rescue system based on an improved active disturbance rejection control (ADRC) method. The UAV employs a tethered power supply to sustain engine operation, enabling precise nozzle deflection and thrust control for enhanced endurance, stability, and payload capacity. A nonlinear dynamic model is established, and an enhanced ADRC is designed by optimising the extended state observer (ESO) with a klnfal function, with its convergence proven via Lyapunov stability theory. Simulations show that under strong disturbances, the improved ADRC reduces attitude control mean square error by 75.81% compared to PID and conventional ADRC, significantly improving robustness for precise material delivery.

Index Terms rescue drone, turbofan engine, tether cable, active disturbance rejection control.

I. Introduction

In recent years, global economic growth and industrial expansion have accelerated the overexploitation of natural resources and environmental degradation, exacerbating the frequency and severity of natural disasters [1]. These catastrophic events often cause severe supply shortages and transportation paralysis, highlighting the urgent need for efficient disaster response solutions. Due to their compact size and manoeuvrability, unmanned aerial vehicles (UAVs) have emerged as vital tools in post-disaster rescue operations. This study focuses on developing an advanced dynamic model for disaster relief UAVs and designing a corresponding flight controller to enhance their operational effectiveness.

At present, many scholars have carried out research in the field of drone rescue. Zitao Du has designed a drone capable of accurately flying to the centre of an accident site while carrying rescue supplies. This drone employs COFDM (Coded Orthogonal Frequency Division Multiplexing) image transmission technology to transmit real-time footage from the scene. [2]. Yijing He proposes a blockchain-based UAV Emergency Rescue Chain (UERChain) that achieves high robustness and reliable collaboration for drone swarm emergency rescue in a weakly decentralised environment through reputation management and faulty node filtering. [3]. Pengzhan Zhang et al. propose improving signal stability of communication equipment at post-disaster sites to develop a transport system for delivering medicines and materials without manual travel [4]. Yongquan Wang et al. used Agisoft Metashape 1.8 and Darknet for disaster mapping and target recognition, summarising a tethered UAV-based emergency mapping method [5]. Li Cong et al. analysed the dynamic response and tension characteristics of a tethered UAV fire hose in a super high-rise building using OrcaFlex 8.7a23, providing critical wind speed data for its firefighting applications. [6]. Ali DINC optimised NOx emissions from a turbofan UAV during surveillance at different speeds and altitudes to improve turbojet emissions control [7]. UAV rescue has potential in emergency response but faces challenges like technological immaturity, environmental adaptability, complex integration, and high skill requirements. The nonlinearity of the UAV model and the sensitivity to external environmental disturbances increase the difficulty of controlling it accurately. In recent years, many scholars have also conducted extensive research in the field of UAV control. Wu Huang et al. employed Proportional–Differential–Integral (PID) control for UAVs, which is convenient and straightforward in design; however, it exhibits weak disturbance suppression and low robustness [8]. Zhu Jiayuan et al. employed Active Disturbance Rejection Control (ADRC), which shows a superior anti-disturbance effect compared to PID; however, it has more parameters, making parameter adjustment a challenging aspect of its control process [9]. Meng et al. proposed an optimal control strategy based on active ADRC, which improved the extended state observer and nonlinear state error feedback and achieved high-precision control of the permanent magnet synchronous motor[10]. This literature has proved that ADRC is superior to PID. Yan Huabiao and other researchers improved the fal function of the extended state observer (ESO) in ADRC, and the modified xfal function has a greater anti-interference effect than the original fal function.

Still, the function does not perform well under the interference of white noise due to the high gain [11]. It can be seen that although PID, ADRC, and methods that improve on them have their advantages in design, they still face common shortcomings, such as a lack of robustness, difficulty in parameter adjustment, and unstable performance under specific interference conditions. Different UAVs are used in rescue operations, but multi-rotor UAVs have low load capacity and are unstable in strong winds. Tethered UAVs enable long-term monitoring, while turbine UAVs can carry heavier cargo and perform stably in complex post-disaster environments[12]. By combining the advantages of two drones, a superior effect can be achieved.

In summary, the innovations presented in this paper are as follows: (1) This work pioneers a novel tethered-turbojet hybrid UAV for disaster relief, uniquely overcoming the endurance-payload-control trade-offs in conventional drones. We establish the first dedicated dynamics model for this original configuration, this innovative model accurately characterizes the flight dynamics of this UAV configuration; (2) An improved *klnfal* function is developed by modifying the *fal* function of the Extended State Observer (ESO), leading to enhanced performance. Furthermore, simulation experiments are conducted to compare the PID, Active Disturbance Rejection Control (ADRC), and the improved ADRC controllers. The results are analysed for errors, and an optimal control design is proposed. This work aims to advance the application of novel UAVs in disaster relief and humanitarian assistance.

II. Establishment of a dynamic uav model

II. A. Principles of Flight

A sketch of the turbojet section of the turbojet tethered UAV proposed in this study is shown in Figure 1 [13]:

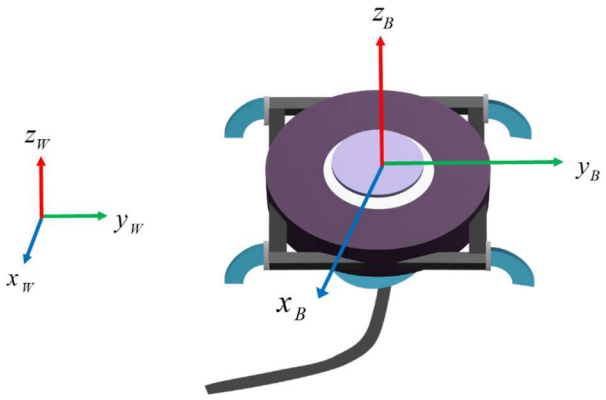

Figure 1: A simplified diagram of the UAV design

The body coordinate system is established with the geometric centre as the origin, defined as the coordinate system $B(X,Y,Z)$, while the inertial coordinate system is defined as $W(X,Y,Z)$. The numbers 1, 2, 3, and 4 are the four rotatable turbojet angles. The thrust vector of the small-thrust turbojet engine can be adjusted by the tail nozzle, as shown in Figure 2, and the angle of rotation can be adjusted only in the X-Z plane of the airframe coordinate system.

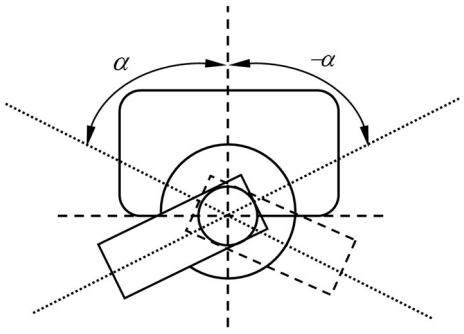

Figure 2: Schematic Diagram of Tail Nozzle Rotation.

In the process of flight, the thrust of the four nozzles is of the same size. This study requires the construction of the rotation matrix R_B^W for coordinate transformation, which can be expressed as follows:

$$R_B^W = \begin{pmatrix} C_\psi C_\theta & C_\psi S_\theta S_\varphi - S_\psi C_\varphi & C_\psi S_\theta C_\varphi - S_\psi S_\varphi \\ S_\psi C_\theta & S_\psi S_\theta S_\varphi + C_\psi C_\varphi & S_\psi S_\theta C_\varphi - C_\psi S_\varphi \\ -S_\theta & C_\theta S_\varphi & C_\theta C_\varphi \end{pmatrix} \tag{1}$$

where denotes $\sin(\cdot)$ and C denotes $\cos(\cdot)$.

During the process of releasing supplies, one only needs to keep the rotation angle of all four nozzles at 90 degrees to enable the drone to fly vertically.

II. B. Modelling of System Dynamics

In reality, the dynamics of UAVs are very complex to model, and for this study, the following assumptions are made for UAVs [13], [14]:

1. The UAV is considered as an absolutely rigid body, without considering its elastic deformation, and the structure is strictly symmetric;
2. The position of the centre of gravity of the body remains constant, and the mass is considered as a constant;
3. The turbojet engine is considered as a whole, and the effect of turbine rotation on the airframe is ignored;
4. The origin in the airframe coordinate system is considered to coincide with the vehicle's centre of gravity.

References [13], [14] established its dynamic model based on the assumption of external structural symmetry for UAVs, an assumption that has been proven reliable. The rescue UAV proposed in this study adopts this assumption from the literature. The incorporated designs of cameras, radar, and other structures are positioned at the internal central location of the UAV, thus not affecting the external structural symmetry. Since the UAV's mass is significantly greater than that of these rescue tools, their influence on the centre of gravity can be neglected. Furthermore, the other assumptions presented herein align closely with the UAV structural conditions detailed in the literature; hence, they are applicable to this paper.

φ, θ, ψ represent the roll angle, pitch angle, and yaw angle, respectively. The thrust of the i turbojet engine in the X, Y, Z directions can be expressed as:

$$F_i^B = [F\sin(\alpha_i), 0, F\cos(\alpha_i)] \tag{2}$$

Then, the total push on the vehicle is

$$F_T^B = \sum_i^4 F_i^B \tag{3}$$

According to Newton's second law, the force of gravity on the vehicle is $F_G^W = [0, 0, -mg]$.

Here, m is the mass of the aircraft, and g is the acceleration due to gravity.

This study adopts the theory of a hanging chain line to analyse the tension situation generated by the cable [15]. It assumes that the angle of the cable connecting one end of the unmanned vehicle is 0, as shown in Figure 3.

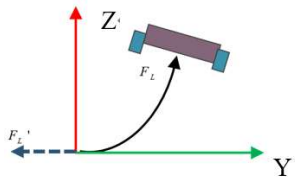

Figure 3: An overall image of the UAV's tethered structure

The tension force is analysed at a point a on the cable, as shown in Figure 4.

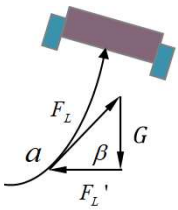

Figure 4: Tension Analysis Diagram at a Point on a Rope

In this paper, the cable rope connected by the UAV belongs to the application scope of the catenary equation, which is basically the same as the cable rope of the tethered UAV in literature 14, and the catenary equation can be used to solve for the tension. According to reference [15], F_L is the tension force generated by the cable on the UAV, F_L' is the tension force generated by the cable on the end of the unmanned vehicle, G is the self-weight of the cable, and β is the angle between the tangent line at point a and the x.

$$\begin{aligned} F_L' &= \frac{x^2 \rho g}{2z} \\ F_L &= \frac{F_L'}{cos\beta} = F_L' \sqrt{1+(\frac{dz}{dx})^2} = F_L' + \rho g z \end{aligned} \tag{4}$$

where x and z are the distances travelled by the UAV in the horizontal and vertical directions from the initial moment minus the distances travelled by the UAV in the horizontal and vertical directions, respectively; ρ is the mass per unit length of the cable; g is the acceleration of gravity.

According to reference [16], this study solves the air resistance force on the cable using the microelement method. The cable in equilibrium is segmented so that the length of each segment is L_i, where L_i denotes the distance from the turbojet engine to the center of gravity of the vehicle and the resistance force is analyzed.

Where F_{fi} is the air resistance of the cable in segment i, which is broken down into resistance in the x-direction F_{fi}^x, y-direction F_{fi}^y, and z-direction F_{fi}^z.

Let the total length of the cable sticking out be S, $n = S / L_i, \left(i = 1,2,\cdots,n\right)$; then, the total air resistance of the cable can be expressed as follows:

$$F_f^W = [F_f^x, F_f^y, F_f^z]^T = [\lim_{n\to\infty}\sum_{i=1}^{n} F_{fi}^x, \lim_{n\to\infty}\sum_{i=1}^{n} F_{fi}^y, \lim_{n\to\infty}\sum_{i=1}^{n} F_{fi}^z]^T \tag{5}$$

In summary, the combined force on the vehicle and the cable is:

$$F = R_B^W F_T^B + F_G^W + F_L^W + F_f^W \tag{6}$$

P^W represents the position vector of the vehicle in the inertial coordinate system; then, the dynamic model of the vehicle position is:

$$m\ddot{P}^W = F \tag{7}$$

Disregarding the effect of cable tension on the torque of the vehicle, the torque of the vehicle is produced by only four small jet engines, the magnitude of which is related to the angle of rotation of the tail nozzle of each engine; for the i turbojet engine, the torque produced can be expressed as follows:

$$M_i^B = L_i^B \times F_i^B \tag{8}$$

where L_i denotes the distance from the turbojet engine to the centre of gravity of the vehicle. According to reference [13], we define the moment of inertia matrix J as a diagonal matrix. The dynamic model of the aircraft's attitude can be expressed as:

$$M_T^B = J\dot{\omega}^B + (\dot{\omega}^B \times J\dot{\omega}^B) \tag{9}$$

where we let the angular velocity $\omega = [p.q.r]^T$.

Introducing the virtual control quantity $U = [U_0, U_1, U_2, U_3, U_4]^T$, with the turbojet engine angle as the actual control quantity, the relationship between the two can be expressed as follows:

$$\begin{pmatrix} U_0 \\ U_1 \\ U_2 \\ U_3 \\ U_4 \end{pmatrix} = \begin{pmatrix} 0 & 0 & 0 & 0 & F & F & F & F \\ F & F & F & F & 0 & 0 & 0 & 0 \\ L_y F & L_y F & -L_y F & -L_y F & 0 & 0 & 0 & 0 \\ -L_x F & L_x F & L_x F & -L_x F & 0 & 0 & 0 & 0 \\ 0 & 0 & 0 & 0 & -L_y F & -L_y F & L_y F & L_y F \end{pmatrix} \begin{pmatrix} \cos(\alpha_1) \\ \cos(\alpha_2) \\ \cos(\alpha_3) \\ \cos(\alpha_4) \\ \sin(\alpha_1) \\ \sin(\alpha_2) \\ \sin(\alpha_3) \\ \sin(\alpha_4) \end{pmatrix} \tag{10}$$

Here, U_0 controls the movement in the direction of the x-axis, U_1 controls the movement in the direction of the y-axis, and U_2, U_3, U_4 control the three rotation angles of roll (φ), pitch (θ), and yaw (ψ), respectively.

Combining Equations (6) and (8), the dynamical rigid body model of the vehicle can be expressed as follows:

$$\begin{cases} \ddot{x} = \dfrac{1}{m}[U_0(C_\psi C_\theta) + U_1(S_\psi S_\varphi + C_\psi S_\theta C_\varphi) + F_f^x - F_L \cos\lambda_1 \cos\lambda_2] \\ \ddot{y} = \dfrac{1}{m}[U_0(S_\psi C_\theta) + U_1(-C_\psi S_\varphi + S_\psi S_\theta C_\varphi) + F_f^y - F_L \cos\lambda_1 \sin\lambda_2] \\ \ddot{z} = \dfrac{1}{m}[-U_0 S_\theta + U_1(C_\theta C_\varphi) + F_f^z - F_L \sin\lambda_1 - mg] \\ \ddot{\varphi} = \dfrac{J_{yy} - J_{zz}}{J_{xx}}\dot{\theta}\dot{\psi} + \dfrac{U_2}{J_{xx}} \\ \dot{\theta} = \dfrac{J_{zz} - J_{xx}}{J_{yy}}\dot{\varphi}\dot{\psi} + \dfrac{U_3}{J_{yy}} \\ \ddot{\psi} = \dfrac{J_{xx} - J_{yy}}{J_{zz}}\dot{\varphi}\dot{\theta} + \dfrac{U_4}{J_{zz}} \end{cases} \tag{11}$$

III. Self-immunity controller design

III. A. Simplification of the UAS Model

Due to the strong nonlinear characteristics of the UAV model, the controller design is more difficult. To reduce the complexity of the design, this study ignored the gyroscopic effect and linearised the UAS model according to the symmetry of the UAV's mechanical structure, with the assumption that the UAV makes a small-angle motion [17].

The simplified model reduces the nonlinearity of the system and the difficulty of control system design. The flowchart of the UAV control system designed according to Equation (12) is shown in Figure 5.

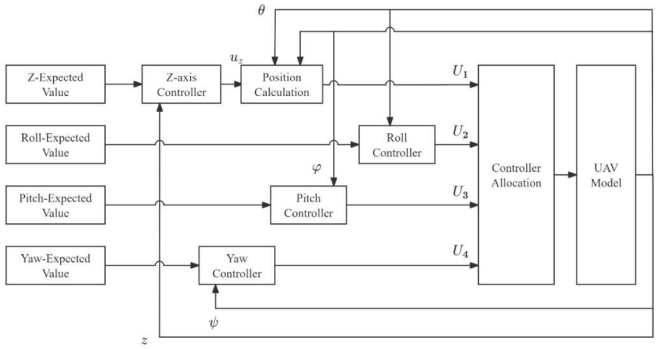

Figure 5: The control flowchart of the UAV

III. B. Positional Self-Immunity Controller Design

Self-immunity controllers generally consist of a tracking differentiator (TD), extended state observer (ESO), and nonlinear state error feedback (NLSEF) [18]. In this study, the z-channel is used as an example to design the nonlinear ADRC controller.

The equation of the z-channel in Equation (12) is selected, and the complex external post-disaster perturbations such as cable tension and wind resistance are considered as total perturbations r_0 so that $r_0 = \frac{1}{m}\left(F_f^z - F_L \sin\lambda_1\right)$; the state variables $z_1 = z, z_2 = \dot{z}$ are chosen to establish the following state space equations:

$$\begin{cases} \dot{z}_1 = z_2 \\ \dot{z}_2 = r_0 + \frac{U_0}{m}(-S_\theta) + \frac{U_1}{m}(C_\theta C_\varphi) - g \\ y = z_1 \end{cases} \tag{12}$$

(1) Tracking Differentiator (TD)

The tracking differentiator is used to arrange the transition process v for the system expectation v_1 to obtain a smooth input signal v_1 and the differential signal of the input signal v_2 This paper is consistent with the tracking differentiator in reference [19].

(2) Extended State Observer (ESO)

ESO is the core part of ADRC and can be used to estimate the system's state and total disturbance.

From Equation (13), r_0 is considered a state that expands into a new state variable z_3, and the new system after expansion is:

$$\begin{cases} \dot{z}_1 = z_2 \\ \dot{z}_2 = z_3 + \frac{U_0}{m}(-S_\theta) + \frac{U_1}{m}(C_\theta C_\varphi) - g \\ \dot{z}_3 = r \\ y = z_1 \end{cases} \tag{13}$$

For this expanded system, the following state observer can be established:

$$\begin{cases} e = z_1 - y \\ \dot{z}_1 = z_2 - \beta_1 fal(e, a_1, \delta) \\ \dot{z}_2 = z_3 - \beta_2 fal(e, a_2, \delta) + \frac{U_0}{m}(-S_\theta) + \frac{U_1}{m}(C_\theta C_\varphi) - g \\ \dot{z}_3 = -\beta_3 fal(e, a_3, \delta) \end{cases} \tag{14}$$

where e is the estimated bias, y is the system output, z_i is the estimated value of each state variable, β_i is the parameter of the controller, δ is a constant, and $fal()$ is a special nonlinear function.

A discretization of the state observer can be obtained as follows:

$$\begin{cases} e = z_1(k) - y(k) \\ z_1(k+1) = z_1(k) + h\left|z_2(k) - \beta_1 fal(e, a_1, \delta)\right| \\ z_2(k+1) = z_2(k) + h\left|z_3(k) - \beta_2 fal(e, a_2, \delta) + \frac{U_0}{m}(-S_\theta) + \frac{U_1}{m}(C_\theta C_\varphi) - g\right| \\ z_3(k+1) = z_3(k) - h\beta_3 fal(e, a_3, \delta) \end{cases} \tag{15}$$

where h is the period of sampling.

(3) Nonlinear State Error Feedback Law (NLSEF)

NLSEF improves PID control by using small gains for significant errors and large gains for minor mistakes, acting as a nonlinear PD control method.

Then, the NLSEF algorithm combined with the $fal()$ function is

$$\begin{cases} e_1 = v_1 - z_1 \\ e_2 = v_2 - z_2 \\ u_0 = \beta_{01} fal(e_1, a_1, \delta_z) + \beta_{02} fal(e_2, a_2, \delta_z) \\ \dfrac{U_0}{m}(-S_\theta) + \dfrac{U_1}{m}(C_\theta C_\varphi) = u_0 - \dfrac{z_3}{a+b} \\ a + b = -\dfrac{S_\theta}{m} \end{cases} \tag{16}$$

where β_{01}, β_{02} are both controller parameters.

III. C. Attitude Controller Design

Taking the yaw angle ψ as an example, the state space equation can be established from Equation (13) as follows:

$$\begin{cases} \dot{\psi}_1 = \psi_2 \\ \dot{\psi}_2 = r_0 + b_0 U_4 \end{cases} \tag{17}$$

Here, $b_0 = \dfrac{1}{J_{zz}}$.

The yaw state observer is similar to the design of the z channel, and can be obtained as:

$$\begin{cases} e = z_1 - y \\ \dot{z}_1 = z_2 - \beta_1 fal(e, a_1, \delta) \\ \dot{z}_2 = z_3 - \beta_2 fal(e, a_2, \delta) + b_0 U_4 \\ \dot{z}_3 = -\beta_3 fal(e, a_3, \delta) \end{cases} \tag{18}$$

The nonlinear error feedback law is similar to Equation (18) and can be expressed as follows:

$$\begin{cases} e_1 = v_1 - \psi_1 \\ e_2 = v_2 - \psi_2 \\ u_0 = \beta_{01} fal(e_1, a_1, \delta_z) + \beta_{02} fal(e_2, a_2, \delta_z) \\ U_4 = u_0 - \dfrac{z_3}{b_0} \end{cases} \tag{19}$$

U_4 is the yaw channel control volume for the final output of the ADRC.

IV. Extended state observer improvements

IV. A. Constructing the klnfal() Function

Considering that the gain parameter of the original *fal* function needs to be adjusted according to the system characteristics, too high or too low a gain will affect the stability and response speed of the system, and it is challenging to choose the gain [20]. Thus, the new *klnfal* function is designed as follows:

$$klnfal(x, k_1, k_2) = \begin{cases} \dfrac{1}{k_1} ln(k_2 x + 1) & x \geq 0 \\ -\dfrac{1}{k_1} ln(1 - k_2 x) & x < 0 \end{cases} \tag{20}$$

where k is the magnitude.

As shown in Figure 6, the gain of the *fal* function at the switching interval is too large, making it easy to cause system jitter. In contrast, the gain of *klnfal* function at the interval switching is smoother, which is very good for achieving the characteristics of a high increase in the small error interval and a low gain in the large error interval. Therefore, bringing the *klnfal* function into the ESO instead of the *fal* function can effectively improve its immunity performance.

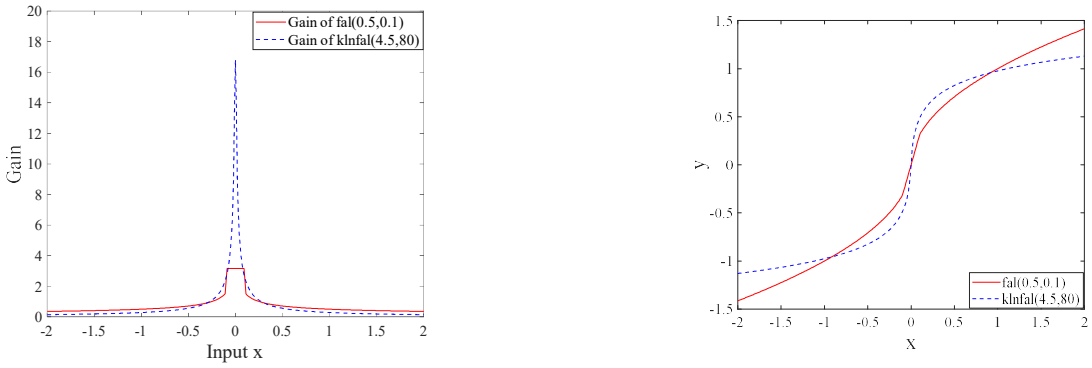

(a) (b)

Figure 6: Comparison of Error Gains of Two Functions and Overall Comparison Chart

IV. B. Convergence Conditions for the Improved Dilated State Observer

Substituting the *klnfal* function into Equation (18) yields the following improved expression:

$$\begin{cases} e = z_1 - y \\ \dot{z}_1 = z_2 - \beta_1 klnfal(e, a_1) \\ \dot{z}_2 = z_3 - \beta_2 klnfal(e, a_2) + b_0 U_4 \\ \dot{z}_3 = -\beta_3 klnfal(e, a_3) \end{cases} \tag{21}$$

Let the system perturbation be 0 to obtain the following expression:

$$\begin{cases} \dot{e}_1 = e_2 - \beta_1 klnfal(e, a_1) \\ \dot{e}_2 = e_3 - \beta_2 klnfal(e, a_2) \\ \dot{e}_3 = -\beta_3 klnfal(e, a_3) \end{cases} \tag{22}$$

This can be further expressed as

$$\dot{e} = -A(e)e \tag{23}$$

In the formula,

$$A(e) = \begin{pmatrix} \beta_1 \dfrac{klnfal(e, a_1)}{e} & -1 & 0 \\ \beta_2 \dfrac{klnfal(e, a_2)}{e} & 0 & -1 \\ \beta_3 \dfrac{klnfal(e, a_3)}{e} & 0 & 0 \end{pmatrix} \tag{24}$$

It is known that if there exists a matrix D such that its central diagonal values are all positive and $DA(e)$ is a positive-definite symmetric matrix. The zero solution of Equation (27) is asymptotically stable in the sense of Lyapunov [21].

Let $F = \dfrac{klnfal(e)}{e} > 0$ be bounded by the definition of the function *Infal*, and let $B = \beta_1\beta_2 F - \beta_3 F$ be bounded. When $B > 0$, the diagonal elements of the matrix D are positive definite so that $DA(e)$ is a symmetric positive-definite matrix [22].

$$D=\begin{pmatrix} 1 & \frac{\beta_2 F}{B}+\mu_1 & -\tau \\ -\frac{\beta_2 F}{B}-\mu_1 & \tau & \frac{1}{B}+\mu_2 \\ \tau & -\frac{1}{B}-\mu_2 & \tau \end{pmatrix} \tag{25}$$

where τ, μ_1, μ_2 are infinitesimal positive numbers.

We take the Lyapunov function of the error system, Equation (26) as follows:

$$V(t)=\int_0^t [DA(e)e, \dot{e}]dt + C = \int_0^t -(\beta_1 e_1 - e_2)^2 - \tau(B_2 F - e_3)^2 - \tau(\beta_3 F)^2 dt + C \tag{26}$$

where $t>0; C$ is a constant.

As τ tends to infinity, we have the following:

$$V(t) \approx \int_0^t -(\beta_1 e_1 - e_2)^2 dt + C \tag{27}$$

At the equilibrium point of Equation (27), $\int_0^t -(\beta_1 e_1 - e_2)^2 dt$ is bounded, so it is only necessary that the constant C be a sufficiently large positive number to make $V(t)>0$. The derivation of Equation is

$$\dot{V}(t) = -(\beta_1 e_1 - e_2)^2 - \tau(B_2 F - e_3)^2 - \tau(\beta_3 F)^2 \tag{28}$$

From the above analysis, it is clear that $V(t) \le 0$; $\dot{V}(t)=0$ if and only if $e=0$. From the above analysis, the system is asymptotically stable at the equilibrium point in the sense of Lyapunov. At the equilibrium point, $F=\frac{klnfal(e)}{e}>0$; then, the system stability condition $B>0$ can be simplified to $\beta_1\beta_2-\beta_3>0$, and the system is asymptotically stable if it satisfies this condition.

V. Simulation study

V. A. Description of Parameters

Multiple experiments were conducted to find the best parameters to ensure that the experimental data can provide a real feedback effect. At the same time, we introduced the *galn* [23] function and the *faln* [24] function, in order to carry out comparative verification to prove the superiority of our improved *klnfal* ,and the relevant parameters are shown in Tables 1–6. After numerous tuning experiments and based on the reference from [15], the following optimal simulation parameters for the controller have been obtained.

Table 1: Drone simulation parameters.

Name	Value	Meaning
m/(kg)	0.65	Mass (in physics)
g/(m/s^2)	9.8	Gravitational acceleration
$J_{xx}/(kg\square m^2)$	0.0552	Moment of inertia about the x-axis
$J_{yy}/(kg\square m^2)$	0.0552	Moment of inertia about the y-axis
$J_{zz}/(kg\square m^2)$	0.1104	Moment of inertia about the z-axis
L/(m)	0.23	Lever arm (i.e., perpendicular distance from the fulcrum of the line of force)
V_i	7.5 × 10-7	Atmospheric drag coefficient

Table 2: Parameters for the TD.

Name/value	h_0	ω
Z	0.05	2
φ	0.05	5
θ	0.05	5
ψ	0.05	2

Table 3: Parameters of the NLSEF.

Name/Value	a_1	a_2	β_1	β_1	δ
Z	0.5	0.05	150	120	3
φ	0.5	0.25	900	100	3
θ	0.5	0.25	150	100	3
ψ	0.5	0.25	200	120	0.04

Table 4: Parameters of the ESO in ADRC with the *fal* function.

Name/Value	a_1	a_2	a_3	β_{01}	β_{02}	β_{03}	δ	b
Z	0.5	0.5	0.5	30	300	1000	0.7	0.9
φ	0.5	0.5	0.5	30	300	1000	0.1	1.5
θ	0.5	0.5	0.5	30	300	1000	0.1	1.2
ψ	0.5	0.5	0.5	30	300	1000	0.1	2.25

Table 5: Parameters of the ESO in ADRC with the *klnfal* function.

Name/Value	K_1	K_2	β_{01}	β_{02}	β_{03}	b
Z	5	100	30	300	1000	0.9
φ	4.5	80	30	300	1000	0.6
θ	4.5	80	30	300	1000	0.9
ψ	4.5	80	30	300	1000	0.67

Table 6: Parameters of the ESO in ADRC with the *galn* and *faln* function

Name/Value	σ_1	σ_2	α_1	α_2
galn	0.5	0.25	*	*
faln	*	*	0.4	0.35

V. B. Experimental design and result analysis

This study evaluates the control performance and disturbance rejection capabilities of each controller primarily based on the methodology established in Reference [11].Building upon the virtual control computation in Equation (10), the dynamic system model in Equation (11), and the ADRC controller architecture established in Sections 3.2–3.3, this study conducts numerical simulations following the workflow illustrated in Figure 5 using the Simulink platform. The implementation details of each controller configuration are elaborated in subsequent sections.

The fixed-step ode4 (Runge-Kutta) solver was selected with a step size of 0.001 s, ensuring the Nyquist frequency (500 Hz) exceeds the highest system dynamics (80 Hz).

The controller's reference commands were configured with: a desired altitude of 2 meters; identical 3-radian attitude angles for pitch, yaw and roll to test multi-axis tracking capability.

Let the initial values of z,ψ,φ,θ be 0, and the expected values are 2, $\frac{3\times180^{\circ}}{\pi}$, $\frac{3\times180^{\circ}}{\pi}$, and $\frac{3\times180^{\circ}}{\pi}$, respectively. The simulation time was 20 s.

The first set of experiments was conducted to observe the error comparison curves of the z, φ, and ψ channels in the three controllers without perturbation, as shown in Figure 7. (a), (b), (c), and (d), respectively, illustrate the responses of the UAV to the PID, ADRC, and improved ADRC control algorithms in the z-axis, roll angle, pitch angle, and yaw angle channels under interference-free conditions.

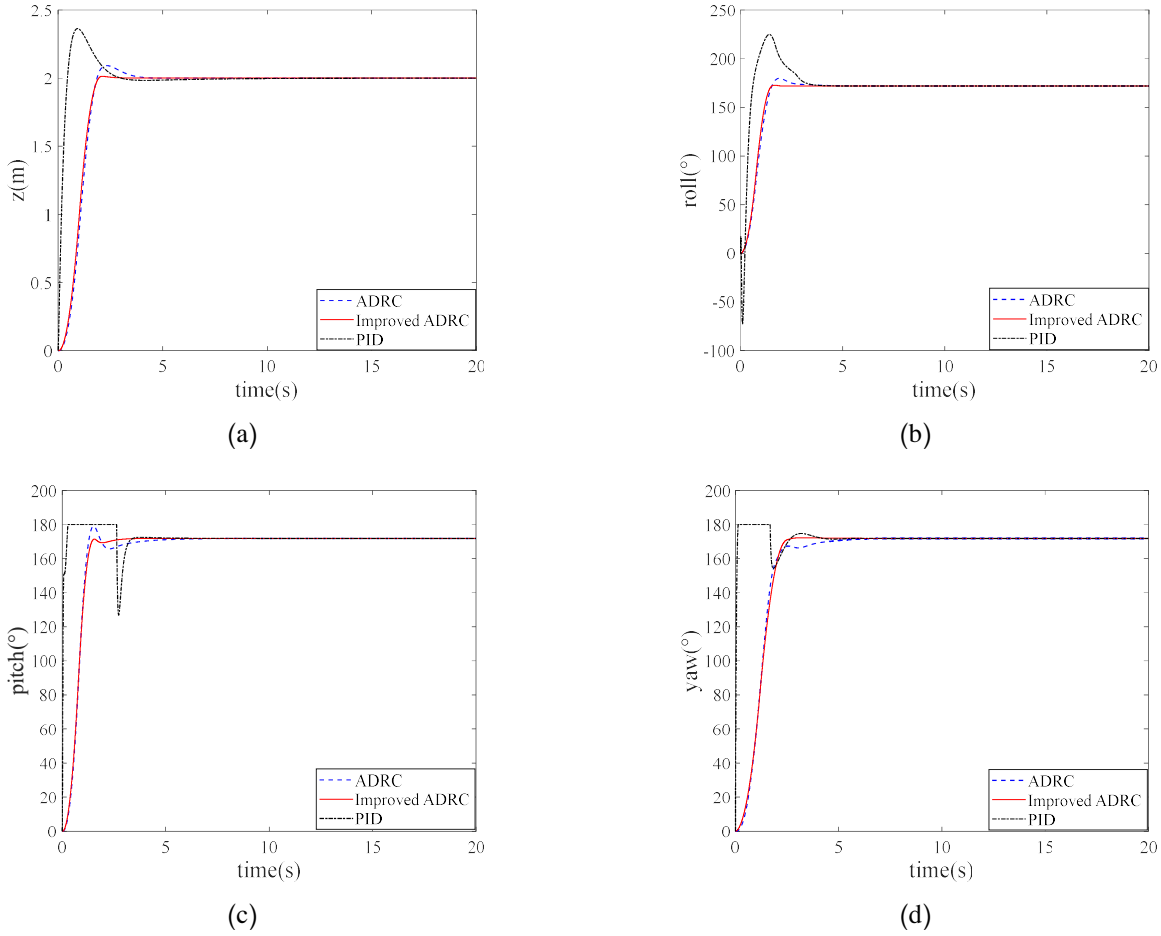

Figures 7: Drone Motion Tracking Errors Without Interference

Since the disturbance in the dynamic model evolves primarily from sinusoidal functions, this paper employs sinusoidal waves to simulate environmental disturbances. The second set of experiments was conducted to observe the error comparison curves of the z, φ, and ψ channels using the three controllers when wind resistance, cable tension, and other perturbations were taken into account, as shown in Figure 8. (a), (b), (c), and (d), respectively, show the responses of the UAV to the PID, ADRC, and improved ADRC control algorithms in the z-axis, roll angle, pitch angle, and yaw angle channels under conditions with disturbances.

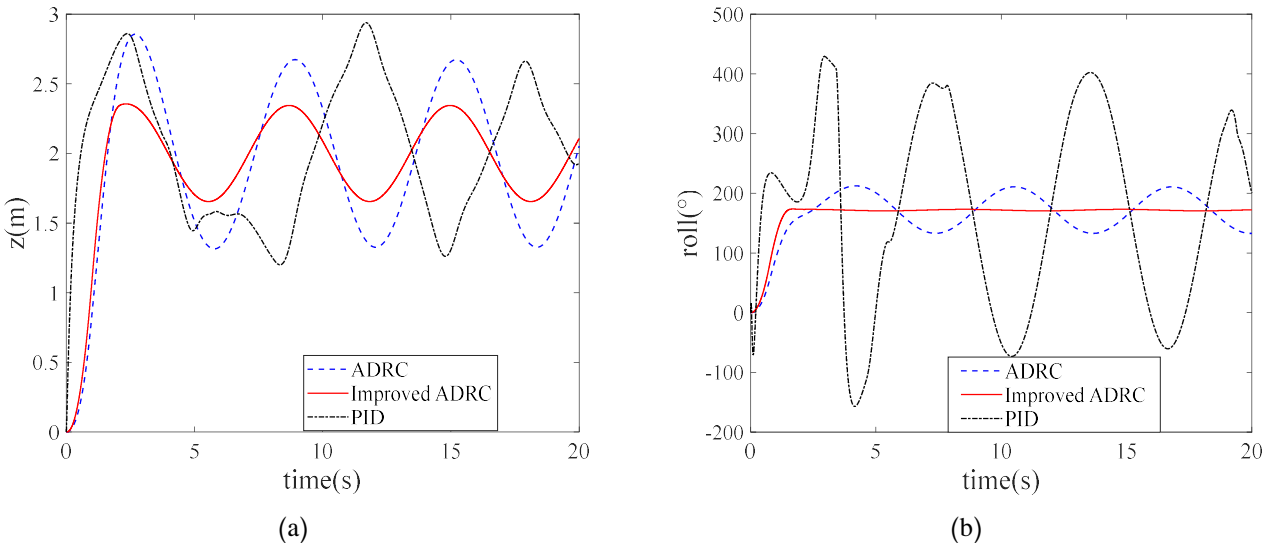

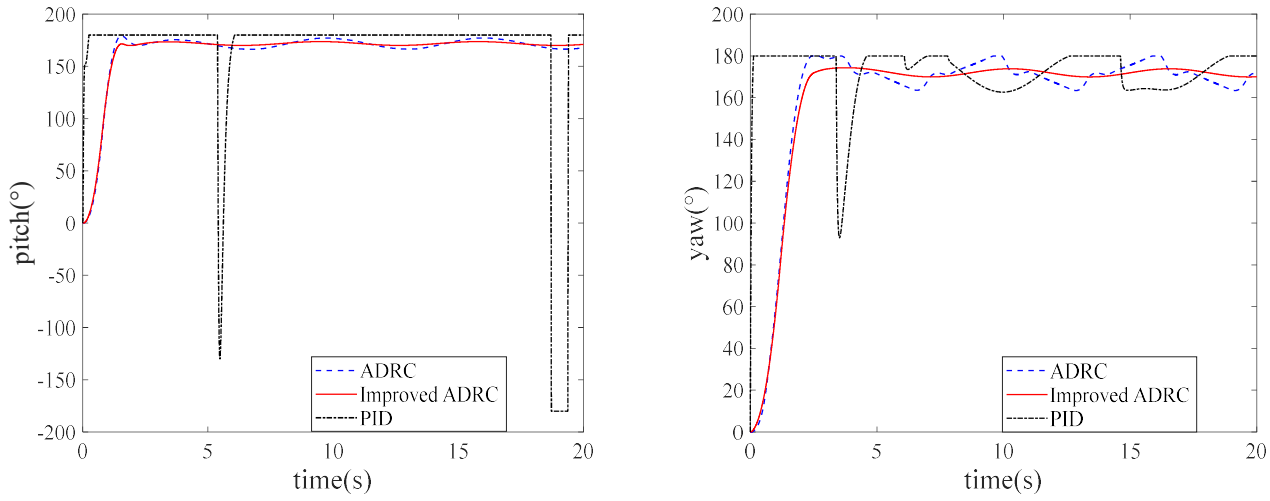

(c) (d)

Figures 8: Drone Motion Tracking Errors With Interference

In order to measure the influence of different controllers before and after the disturbance of the UAV during material delivery in actual disaster relief, this study calculated the mean square error of the z -axis for the exact height and the desired height. The MSE value was taken as the following fluctuation index:

$$MSE = \frac{1}{N}\sum_{i=1}^{N}(\hat{y}_i - y_i)^2 \tag{29}$$

where N is the number of samples, $\hat{y}_i$ is the first desired height i, y_i is the first actual height i, and the time taken is 1.7 s–20 s; the results of the calculation of the mean square error are shown in Table 7.

Table 7: Mean square error of the controllers.

Controllers	Interference-Free	Interference
PID	0.000517307	0.254238685
ADRC	0.000412806	0.249322961
Improved ADRC(klnfal)	0.000036874	0.060314116
galn ()	0.000051432	0.071657218
faln ()	0.000065781	0.249879415

This study adopted the convergence time as the basis for judgment, as shown in Table 8, to compare the rate of UAV convergence to the desired value when using different controllers without interference.

Table 8: The time taken for the controller to converge to the desired value.

Controllers	Time
PID	20s or more
ADRC	10.112 s
Improved ADRC(klnfal)	6.907 s
galn ()	7.115s
faln ()	7.561s

With the comparison in Figure 7, it can be seen that the ADRC before and after the improvement can provide better attitude control and effective tracking of the tethered turbojet UAV when the UAV is undisturbed; however, the ADRC with *klnfal* is slightly inferior to the original ADRC in terms of the amount of overshooting and the speed of convergence, and there is a

more pronounced overshooting phenomenon in the PID during the rising period. As shown in Figure 7c,d, the PID has sudden large fluctuations, low curve smoothness, and poor control performance. According to Table 7, the mean square error of ADRC with *klnfal* is reduced by about 75.81% compared with the original case, and mean square error is lower than that of the *faln* and *galn* functions. At the same time, the jitter generated by it is obviously lower, which indicates that it can effectively reduce the jitter. According to Table 8, the ADRC with *klnfal* has the shortest convergence time, followed by the *faln* and *galn* function, and PID has the longest convergence time and exceeds the time range selected for the experiment, which shows that the convergence rate of the improved ADRC increases significantly.

In the comparison in Figure 8, it can be seen that when the UAV is subjected to external disturbances, the ADRC with *klnfal* effectively suppresses the effects generated by the external disturbances, which is particularly evident in Figure 8b. This is due to the fact that *klnfal* has a high gain in the low error interval and an appropriately low gain in the high error interval, which enables the ESO to provide a more accurate estimation and compensation of the disturbance. The overshooting phenomenon in PID is more serious, as shown in Figure 8c, as it is unstable and prone to significant sudden changes in the control process. In Table 7, it can be seen that the performance of the *klnfal* function in disturbance height compensation is much better than that of the *fal* and *faln* function, and a bit better than the *galn* function, but if the disturbance turns a square wave, the *galn* function goes haywire, which means that the upgraded *klnfal* function works better at suppressing disturbances and overshooting in drone control than original *fal*, *galn*, and *faln* functions. Consequently, the improved ADRC with *klnfal* function has a faster convergence speed, making it more conducive to the control of UAVs in the process of material dropping.

VI. Conclusions

This study was conducted mainly to address the inconvenience and danger of post-disaster rescue, taking into account the characteristics of different kinds of UAVs; the goal was to design a new tethered turbojet UAV with the characteristics of long endurance, high payload, stable work, and the ability to take off and land vertically. The study established a dynamic model for the UAV; used Simulink to simulate and analyze the rescue process, including material placement and attitude change; improved the ADRC, established the *klnfal* function; and compared the control performance of the UAV with PID, ADRC, and ADRC controllers with the improved *klnfal* function when it is not interfered with and when it is interfered with by a complex environment. It was found that the control performance of *klnfal* is the best, with good anti-interference ability. It can be seen that this tethered turbojet UAV can be a key technological tool in future post-disaster rescue missions, such as material delivery, helping to improve rescue efficiency and reduce personnel risk.

In the future, the improved *klnfal* function can be integrated with intelligent control algorithms (e.g., fuzzy control, genetic algorithms) to enhance UAV adaptability and accuracy in complex environments. Additionally, by combining it with sensor technology and artificial intelligence, UAVs can develop real-time environmental sensing systems, automatically adjust mission strategies, and improve intelligence in rescue operations, leading to faster and more precise responses.

Declaration of conflicting interests

The author(s) declared no potential conflicts of interest with respect to the research, authorship, and/or publication of this article.

Data sharing agreement

The datasets used and/or analyzed during the current study are available from the corresponding author on reasonable request.

Funding

The author(s) received no financial support for the research, authorship, and/or publication of this article.

References

[1] Zichen Zhou, Xianbin Wang. An all-terrain plant resource detection and positioning system for post-disaster forest land based on UAV technology. Electronic measurement technology, 2025, 48(07):192-197. DOI:10.19651/j.cnki.emt.2518115.

[2] Zitao Du, Chun Liu, Zhihao Zhang. The Design and Implementation of a Rescue Drone Based on Target Recognition. Control Engineering of China, 2021, 28(11):2174-2177. DOI:10.14107/j.cnki.kzgc.20210057.

[3] Yijing He, Wei Yang. Autonomous Pose Estimation for Underground Post-Disaster Rescue Drones Based on Visual and Laser Fusion. Industrial and Mining Automation, 2024, 50(04):94-102. DOI:10.13272/j.issn.1671-251x.2023080124.

[4] Pengzhan Zhang, Leng Zhang, Fangzheng Li, Danbei Wang, Ling Zhang, Kongping Wu. Design of emergency rescue system based on multi-rotor UAV. Electronic technology, 2024, 53(08):188-189.

[5] Yongquan Wang, Qingquan Li, Chisheng Wang, Jiasong Zhu, Xinyu Wang. Application of emergency mapping technology based on tethered UAV. Geological land resources remote sensing, 2020, 32(01):1-6.

[6] Cong Li, Zhuoqi Wu, Gaohao Yang, Lele Hou, Rui Zhou. Attitude response of tethered unmanned aerial vehicle (UAV) tethered to a flexible pipe cable under the consideration of ambient wind speed and offset distance. Engineering mechanics, 2025, 1-9. DOI:http://kns.cnki.net/kcms/detail/11.2595.O3.20241021.0943.002.html.

[7] Ali, DINC. NOx emissions of turbofan powered unmanned aerial vehicle for complete flight cycle. Chinese Journal of Aeronautics, 2020, 33(06):1683-1691.

[8] Lingfeng Huang, Yifan Li, Zhou Kun, Qi Xiao, Rongyun Ma. A UAV Control Method Based on PID Iterative Learning. China Science and Technology Information, 2024, (08):12, 121–124.

[9] Jiayuan Zhu, Zhong Yang, Changliang Xu, Jie Xu, Jingsong Li. Research on self-immunity flight controller for quadrotor UAV. Applied technology, 2019, 46(01): 29–35+42.

[10] Yibo Meng, Bingyou Liu, Lichao Wang. Speed control of PMSM based on an optimized ADRC controller. Mathematical Problems in Engineering, 2019,20191-18.https://doi.org/10.1155/2019/1074702

[11] Huabiao Yan, Weibin Xu, Lve Huang. Design of quadrotor attitude controller based on improved ADRC. Journal of Beijing University of Aeronautics and Astronautics, 2023,49(12):3283-3292. DOI:10.13700/j.bh.1001-5965.2022.0129.

[12] Chao Qi, Fengyi Zhou. Exploration of vehicle-mounted tethered UAV low-altitude monitoring platform. China Radio, 2024, (08): 47–49.

[13] Yankai Yin. Research on Key Technology of Turbojet-Powered Aircraft for Post-Disaster Rescue. Nankai University, 2024. DOI:10.27254/d.cnki.gnkau.2024.000018.

[14] Zhijun Liu, Qiang Lv, Donglai Wang. Modelling and simulation control of a small quadrotor helicopter. Computer simulation, 2010,27(07):18-20+69.

[15] Zhan Zhou, Zhigang Chen, Xiao Li, Haoxiang Su. Design of tethered UAV self-immunity controller based on parameter rectification. Journal of Southwest University of Science and Technology, 2024, 39(04):100-109. DOI:10.20036/j.cnki.1671-8755.2024.04.013.

[16] Hui Zhang. Research on Fault Tolerant Control of Quadcopter UAV Based on Anti-Slip Synchronous Modelling Algorithm. Northeast Agricultural University, 2021. DOI:10.27010/d.cnki.gdbnu.2021.000330.

[17] Wei Wei, Yan Wu, Fang Li, Lifang Wang, Junzhi Zhang. Trajectory tracking control of quadrotor UAV based on improved self-immunity. New technology of electrician electricity, 2023, 42(05):1-13.

[18] Haishuang Guan, Jianmin Zhang, Yanyu Meng. Control strategy of magnetic levitation bearing based on linear self-immunity control. Journal of North China University of Technology (Natural Science Edition), 2020, 21(05):675-681.

[19] Pei Zhan, Haifeng Xiao. Control of robustness of second-order self-resilient speed control system for permanent magnet synchronous motor. Electromechanical information, 2021, (24):6-7+10. DOI:10.19514/j.cnki.cn32-1628/tm.2021.24.003.

[20] Xingyong Liao, Zhi Li. Research on helicopter attitude control based on improved fal function ADRC algorithm. Electronic production, 2024, 32(07):108-112+22. DOI:10.16589/j.cnki.cn11-3571/tn.2024.07.029.

[21] Martin Gugat. New Lyapunov functions for systems with source terms. Control and Cybernetics, 2025, 53(1):163-187.

[22] Tao Zhou. Expanded state observer based on inverse hyperbolic sine function. Control and decision-making, 2015, 30(05):943-946. DOI:10.13195/j.kzyjc.2014.0316.

[23] Zhiwang Chen, Zizhen Zhang, Yujie Cao. Fal function improvement of ADRC and its application in quadrotor aircraft attitude control.Control and Decision, 2018, 33(10):1901-1907. DOI:10.13195/j.kzyjc.2017.0606.

[24] Wenqi Yang, Jianhua Lu, Xu Jiang, Yuanxin Wang. Design of quadrotor attitude active disturbance rejection controller based on improved ESO. Systems Engineering and Electronics, 2022,44(12):3792-3799.